CHEMISTRY
A European Journal

A Journal of
ChemPubSoc Europe

Accepted Article

Title: Synthesis of Size-tunable Hollow Polypyrrole Nanostructures and Their Assembly into Folate Targeting and pH-responsive Anti-cancer Drug Delivery

Authors: Jian Chen, Xiufang Li, Yanhua Sun, Yuwei Hu, Yulong Peng, Yimin Li, Gang Yin, Hui Liu, Jiangfeng Xu, and Shian Zhong

To be cited as: *Chem. Eur. J.* 10.1002/chem.201702945

Link to VoR: http://dx.doi.org/10.1002/chem.201702945

Supported by
ACES

WILEY-VCH

10.1002/chem.201702945

Synthesis of Size-tunable Hollow Polypyrrole Nanostructures and Their Assembly into Folate Targeting and pH-responsive Anti-cancer Drug Delivery

Jian Chen[1], Xiufang Li[1], Yanhua Sun[1], Yuwei Hu[1], Yulong Peng[2], Yimin Li[2], Gang Yin[2,**] ,Hui Liu[1], Jiangfeng Xu[1], Shian Zhong[1,*]

[1]College of Chemistry and Chemical Engineering, Central South University, Changsha Hunan, 410083, P.R. China

[2]School of Basic Medical Science, Central South University, Changsha, Hunan, 410083, P.R. China

*Corresponding author. College of Chemistry and Chemical Engineering, Central South University, Changsha Hunan, 410083, P.R. China

E-mail: zhongshian@aliyun.com

**Co-corresponding author. School of Basic Medical Science, Central South University, Changsha, Hunan, 410083, P.R. China

E-mail: gang.yin@csu.edu.cn

ABSTRACT

Chemotherapeutic drugs currently used in clinical settings have a high toxicity, low specificity, and short half-life. Herein, polypyrrole (PPy)-based anticancer drug nanocapsules were prepared by tailoring the nanoparticles size with a template method, controlling drug release by aromatic imine, increasing nanoparticles stability through PEGylation, and improving tumor cell selectivity via folate (FA) mediation. Nanoparticles were characterized by transmission electron microscopy (TEM) and dynamic light scattering (DLS). α-folate receptor (α-FR) expression level between tumor cells and normal cells was investigated by western blot and quantitative polymerase chain reaction (qPCR) analyses. Flow cytometry and fluorescence imaging were used to verify the cell uptake of the different size nanoparticles. In terms of different size polypyrrole nanoparticles, the optimal functionalized nanoparticles of 180 nm hydrodynamic size were chosen and further used *in vitro* and *in vivo* tests. The nanoparticles showed excellent biocompatibility and the drug-loaded nanoparticles exhibited effective tumor cell growth inhibition *in vitro*.

Moreover, the drug-loaded nanoparticles showed a substantially enhanced accumulation in tumor regions and effectively inhibited *in vivo* tumor growth. Furthermore, the nanoparticles showed reduced doxorubicin (Dox) -induced toxicities and led to no significant side effects in normal organs of tumor bearing mice as measured by body weight shifts and drug distribution evaluation. Overall, the functionalized nanoparticles are a promising nanocarrier candidate for tumor targeting drug delivery.

Keywords: polypyrrole, nanotube, drug carrier, tumor, folate

INTRODUCTION

With recent developments in nanobiotechnology, novel nanoparticles have gained increasing attention as nanodevices for application in cancer therapy[1]. Drug encapsulation within nanoparticles offers various advantages, including efficiently controllable and targeted drug delivery as well as a reduction in adverse effects. It is well-known that nanoparticles size and surface properties play a key role in determining their *in vivo* fate[2]. Defective tumor tissue, which contains gap ranging from 100 to 1000 nm, favors nanoparticles permeation. However, healthy tissues are regular and have tight intercellular junctions of less than 10 nm[3]. Therefore, certain size drug delivery nanocarriers are able to selectively leak into tumor tissue but cannot be transported into healthy tissue. Therefore, polymeric nanoparticles of less than 200 nm can easily escape the reticuloendothelial system (RES), thus be able to passively accumulate in tumor tissues due to the enhanced permeation and retention (EPR) effect[4]. Furthermore, nanoparticles smaller than 200 nm can prolong the *in vivo* circulation time and enhance drug bioavailability[5]. Besides, actively targeted drug delivery has emerged as a significant method to transport antitumor drugs to specific tumor sites and decrease the internalization of drugs within normal tissues, thus reducing side effects and improving the clinical efficiency[6]. In order to further improve the accumulation of nanocarriers at the tumor sites, their surface is commonly functionalized with targeting ligands, such as antibodies[7], polypeptides[8], and FA[9], which have been proved to selectively bind to the overexpressed receptors on the surface of tumor cells[10]. Normal cells usually also express such receptors but

just at a lower level. Analogously, FA (vitamin B9) is involved in 1-carbon transfer reactions essential for RNA and DNA synthesis. Moreover, the FR is a glycosylphosphatidylinositol-anchored membrane protein that transports FA into the cell. FR is differentially expressed in normal and tumor tissues. α-FR, the most extensively studied family member, is generally expressed in urogenital organs, the female genital tract, and the placenta. However, high α-FR level have been detected in different carcinomas, including non-mucinous ovarian carcinoma, endometrial carcinoma, and cervix carcinoma[11], as well as in non-genital tumors, and are related to elevated tumor cell cycle progression and proliferation. Therefore, the high expression of α-FR in cancer cells and the high affinity of FR for FA have led to extensive researches, which concern its potential role as a target for chemotherapy and as a diagnostic marker in tumor imaging[12].

PPy is an excellent electroactive polymer, which is commonly used for nerve regeneration[13], drug delivery[14], and other biological applications[15], given its excellent biocompatibility[16]. PPy materials applied in cancer therapy are in its primary stage and lead to a breast of research activities. Tang et al. prepared spindle-like polypyrrole hollow Nanocapsules for chemo–photothermal combination therapy of cancer cells in Vivo[17]. Wang et al. synthesized near-infrared light and pH-responsive polypyrrole@polyacrylic acid/fluorescent mesoporous silica nanoparticles for imaging and chemo-photothermal cancer therapy[18]. Zare et al. studied polypyrrole nanoparticles for tunable, pH-sensitive and sustained drug release[19]. The reported PPY-based nanoparticles focus on chemo/photothermal synergistic therapy combining pH-/photoresponsive drug release, which is very helpful for the development of efficient anticancer strategy. Given their large inner volume, nanotubes offer advantages over sheet, rod, and spherical nanoparticles with regard to the transport of drug molecules[20]. Meanwhile, a number of methods have been demonstrated to generate hollow PPy nanostructures, while the most versatile one is based on template-directed synthesis[21]. As well as determining the morphology of the prepared nanotubes, the template approach offers control of the dimensions of nanotubes fabrication[22]. The surface of a template, such as a porous

membrane, can be directly coated with a layer of oxidants to initiate polymerization. The main advantages of the template approach are its adaptability to large-scale fabrication and the tailorability of the diameter of the PPy nanotubes through the use of templates with various diameters. Meanwhile, given the ease of preparation of PPy and the flexibility of its surface characteristics, targeting ligands attach onto suitably sized nanoparticles to achieve both active targeting via the conjugation of receptors and passive targeting via enhanced permeation and retention effect[23]. In addition, nanoparticles may be tailored through the use of physical or chemical stimuli responsiveness, including pH[24], light[25], redox[4], and enzymes[26], to exploit a series of cellular drug release mechanisms. Among the various stimuli, pH responsivity is frequently utilized since pH values vary in different tissues and cellular compartments. The tumor extracellular environment is more acidic (pH 6.2–6.9) than blood and normal tissues (pH 7.3–7.4), and even more so in cellular endo/lysosomes (pH 4.0–6.0)[24b, c]. The aromatic imine bond, easily formed by amidogens and aromatic aldehydes[24a], is stable under neutral and alkaline conditions but becomes labile with an acidic trigger. Therefore aromatic imine bond is an ideal pH-sensitive bond for tumor environment.

The main objective of the present study was to investigate the effects of particle size of polymeric nanoparticles functionalized through surface modification on cellular uptake. Tubular PPy with tunable 60-200 nm diameters were successfully synthesized using a TiO_2 nanotubes array template in the presence of $FeCl_3$ and pyrrole monomer. Aromatic imine bonds were introduced into the PPy nanoparticles through reaction with tetra-arm aldehyde (TAA) to prepare a novel pH-triggered cleavable backbone. A hydrophilic or amphiphilic surface coating, such as polyethylene glycol (PEG), was added to solubilize the carrier, thus further prolonging the nanoparticles suspension time *in vivo* and reducing systemic clearance. One end of PEG was functionalized with FA as the targeting ligand to bind with α-FR on the tumor cell surface, whereas the other end was chemically conjugated to the surface of PPy nanoparticles via a cleavable aromatic imine bond to control release of drug. Flow cytometry and fluorescence microscopy were used with commercially

available fluorescent tagged PPy nanoparticles in the evaluation of particle size effects on cell endocytosis *in vitro*. Guided by the optimal size of PPy nanoparticles, the therapeutic efficacy of Dox-loaded PPy nanoparticles was demonstrated both *in vitro* and *in vivo*. The overall procedure for size-tunable PPy nanotubes synthesis combining with pH-triggered drug release and α-FR targeting was designed for targeted drug delivery to tumor tissues (Scheme 1).

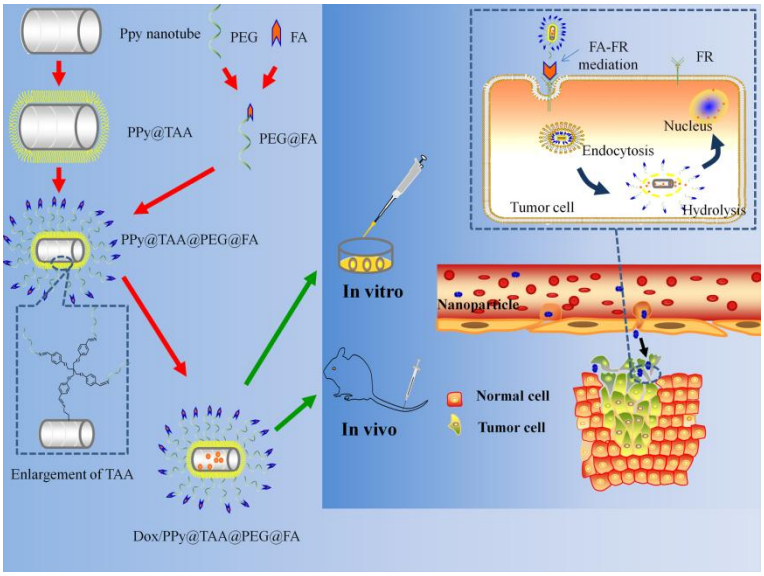

Scheme 1. Schematic illustration of PPy-based drug delivery system responding to mildly acidic tumor tissues.

RESULTS AND DISCUSSION

Synthesis and Characterization of PPy@TAA@PEG@FA. The detailed synthesis protocol of PPy@TAA@PEG@FA is shown in Scheme 1 and Supporting Information (Figure S1-S5). PPy nanotubes were initially prepared via chemical polymerization of 1-(2-aminoethyl)pyrrole (Supporting Information, Figure S 1) through a template method. Figure 1 (a) shows the TEM images of the synthesized PPy nanotubes within the pores of the TiO_2 template membrane. The dimensions of the PPy nanotubes were tailored in accordance with the diameter of the TiO_2 template used. PPy nanotubes of 60, 98, 120, 170, and 200 nm in diameter were obtained. The synthesis and characterization of the TiO_2 template were detailed in Figure 1 (a) and Supporting Information (Table S 1)[27].

PPy/PEG nanoconstructs were engineered by conjugation of the intermediate TAA through a aromatic imine bond. Aromatic imine bond formation was difficult in the acidic environment, which introduced a dynamically pH-sensitive manner. TAA, formed through the reaction of pentaerythrityl tetrabromide(Supporting Information, Figure S 2)[28] with p-hydroxy benzaldehyde[29], is a four-arm aldehyde (Supporting Information, Figure S 3). TAA plays an essential role in the controlled release of drugs and in the formation of a hydrophobic layer. One arm of TAA was attached onto the PPy nanotubes backbone, while the remaining three arms were present at the end of the PEG or FA@PEG (Supporting Information, Figure S 4) chains. The aldehyde group of TAA reacted with the amino group of PPy surface to form aromatic imine bond. Consequently, the TAA was coupled with PPy, as shown in enlargement of TAA in Scheme 1.The star-branched linker (TAA) was designed to increase the proportion of PEG on the PPy nanotubes surface. The overall functionalization of the nanoparticles was considered to act as visualized microcapsules for drug encapsulation and additionally as drug delivery.

The surface functionalization of PPy was characterized by Fourier Transform Infrared Spectroscopy (FT-IR, Figure 1 (b)) and Thermaogravimetric analysis (TGA, Figure 1 (c)). At the beginning of polymerization, the pyrrole monomer was modified with an amino group, namely 1-(2-aminoethyl)pyrrole[30]. The FT-IR spectrum of PPy showed a C–H stretching vibration at 2920 $cm^{-1}$and a N–H stretching vibrations at 3452 cm^{-1}, thus confirming that the amino ethyl group was retained on the PPy surface. Peaks at 1639 and 1480 cm^{-1} were associated with the C–C and C–N stretching vibrations of the PPy ring. The surface of PPy was first functionalized with TAA to obtain PPy@TAA. The presence of the aromatic aldehyde group on the PPy surface was confirmed by two symmetrical peaks, one at 2827 cm^{-1} and another at 2728 cm^{-1}, representing the C–H stretching vibration of CHO. The peak at 1688 cm^{-1} was assigned to the C=N stretching vibration of the aromatic imine bond. Peaks at 1604, 1570 and 1507 cm^{-1}could be ascribed to benzene C=C vibration of TAA and the peak of 3071 cm^{-1} could be assigned to the benzene C-H vibration of TAA. A characteristic peak at 2920 cm^{-1} was due to an overlap of the alkane segment of PPy

and TAA. For PPy@TAA@PEG, the C-O ether absorption bands at 1267, 1183, 1135, and 1068 cm^{-1} confirmed the existence of PEG. In comparison, the spectra of PPy@TAA@PEG@FA showed a significant increase in adsorption at 3076 and 3119 cm^{-1}, which could be attributable to the absorption O-H of COOH group and N-H of NH_2 group of FA as a result of the conjugation of FA on PEG. The characteristic peaks at 1742, 1508 and 1441 cm^{-1} corresponded to the C=N, C=O and C-N stretching bands of FA. Furthermore, a slight shift in peak positions and the additional number of peaks also suggested the presence of FA.

The successful functionalization of the nanoparticles was further confirmed by TGA (Figure 1 (c)). The weight losses of PPy, PPy@TAA, PPy@TAA@PEG and PPy@TAA@PEG@FA from 100 to 900 ℃ were 53.5%, 60.4%, 70.4% and 71.3%, respectively. For PPy, there was no significant mass loss from 100 to 300 ℃. Major weight loss began at 400 ℃, possibly due to the decomposition of PPy[31]. The turning point at 600 ℃ was possibly ascribed to the breakdown of aminoethyl group grafted on the PPy surface. For PPy@TAA, the weight loss percentage was 6.9% larger compared to PPy, indicating that TAA was successfully immobilized onto the surface of the nanotubes. For PPy@TAA@PEG and PPy@TAA@PEG@FA, a faster decomposition was observed compared to PPy and PPy@TAA due to PEG degradation occurring at 300 ℃[32]. Given the similarities between PEG and PEG@FA, no significant mass loss differences were observed between PPy@TAA@PEG and PPy@TAA@PEG@FA.

The component analysis of the sample was carried out using X-ray photoelectron spectroscopy (XPS, Figure 1 (d)). The coexistence of C,N and O elements was evidenced by the main peaks at 284, 400 and 532 eV. The O_{1S} spectra of PPy might be derived from surface adsorbed water. The relatively atomic ratio of C:N:O, which could express the material composition from PPy to PPy@TAA, PPy@TAA@PEG and PPy@TAA@PEF@FA. The data analysis was carried out using XPS PEAK41 software by least-sqares fitting of Gaussian-Lorentzian lineshapes to the photoelectron peaks after subtracting a Shirley background, as shown in Figure S 6 [33].The C_{1S} spectra of PPy could be divided into two peaks: C-N of PPy at 285.43 eV

and C=C of PPy at 284.53 eV. The C_{1S} spectrum of PPy@TAA was fitted into three contributions, which could be assigned to C-O of TAA and C=C of PPy@TAA at 284.5 eV, C-N of PPy and C=N of PPy@TAA at 286.02 eV and C=O of TAA at 287.1 eV. The C_{1S} spectrum of PPy@TAA@PEG exhibited two resolved doublets, resulting from C-C and C-O-C of PEG located at 283.8 eV and 285.3 eV and the C_{1S} spectra of PPy and TAA could still be fitted[34]. The shift in peak pattern of PPy@TAA@PEG when comparing the C_{1S} spectrum of PPy@TAA provided evidence of the composition. The C_{1S} spectra of PPy@TAA@PEG@FA could be separated into four peaks. The two main peaks, present at 283.7 and 285.01 eV, were characteristic peaks of PEG. The other two peaks with a lower intensity, located at 284.5 and 286.01 eV, were due to C element of PPy and FA. It was worth noting that one characteristic peak belonged to several species, whose chemical environment were too close. The binding energy N_{1S} peak of PPy at 399.52 and 400.97 eV were due to NH_2 and C-N-C of PPy. Comparing to N_{1S} peak of PPy, the N_{1S} peaks of PPy@TAA had a C=N (402.01 eV) signal and exhibited a large distribution. There was NH_2 signal in N_{1S} spectra of PPy@TAA that was related to unreacted NH_2 group with aromatic aldehyde group. The similar trend could be seen for N_{1S} spectra of PPy@TAA@PEG and PPy@TAA@PEG@FA. The increase of the signal at 402.09 eV for N_{1S} spectra of PPy @TAA@PEG@FA could attribute to FA. The O_{1S} fitting of PPy@TAA was obtained due to C=O of TAA at 530.98 eV and C-O-C of TAA at 532.01 eV. The bing energy at 531.94 eV of PPy@TAA@PEG when comparing PPy@TAA provided evidence of C-O-C signal of PEG. O_{1S} peak of PPy@TAA@PEG@FA became much broadened and could be overlapping at 531.5 eV assigned to C=O of TAA and COO^- of FA, and at 532.98 eV assigned to C-O-C of PEG and OH of FA.

The hydrodynamic diameter of PPy nanoparticles following hydrophilic PEG coating in an aqueous medium was assessed. The hydrodynamic particle size and the zeta potential of PPy (I, II, III, IV, and V), PPy@TAA (I, II, III, IV, and V), PPy@TAA@PEG (I, II, III, IV, and V), and PPy@TAA@PEG@FA (I, II, III, IV, and V) were measured by DLS (the results are presented in Supporting Information Figure S 7 (a) and Table S 2). The PPy and PPy@TAA nanoparticles were highly

10.1002/chem.201702945

agglomerated prior to PEG or PEG@FA functionalization (Figure S 7 (b)). Following surface modification by PEG or PEG@FA, the obtained nanoparticles were homogeneously suspended in a PBS solution (Figure S 7 (b)), with the hydrodynamic size of the nanoparticles being reduced universally from the micro- to the nano-scale (Figure S 7 (a)). As shown in Table S 2, the reversed change in zeta potential of PPy@TAA was relative to the incorporation of TAA in comparison with pure PPy. The zeta potential of PPy@TAA@PEG and PPy@TAA@PEG@FA fell within -20 to -40 mV, indicating the successful introduction of PEG or PEG@FA groups.

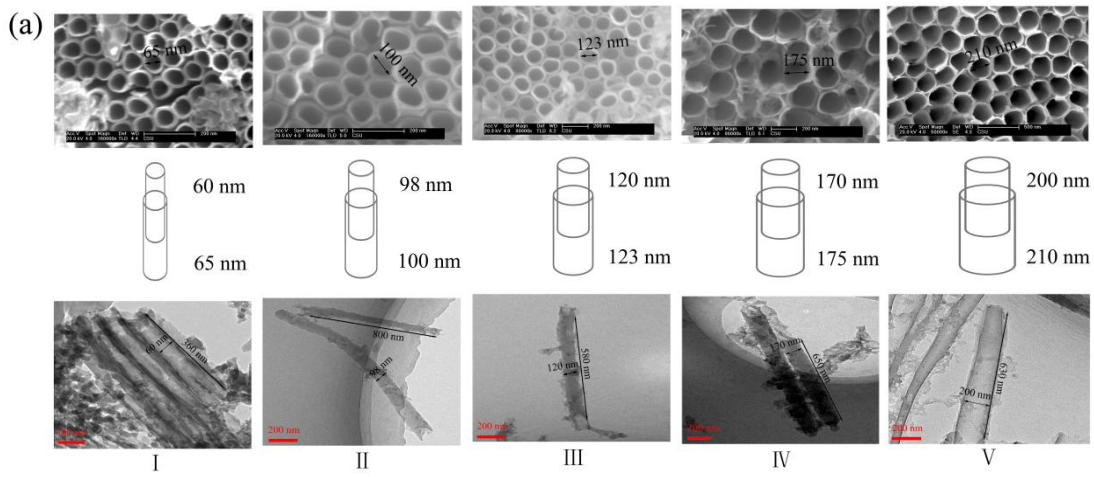

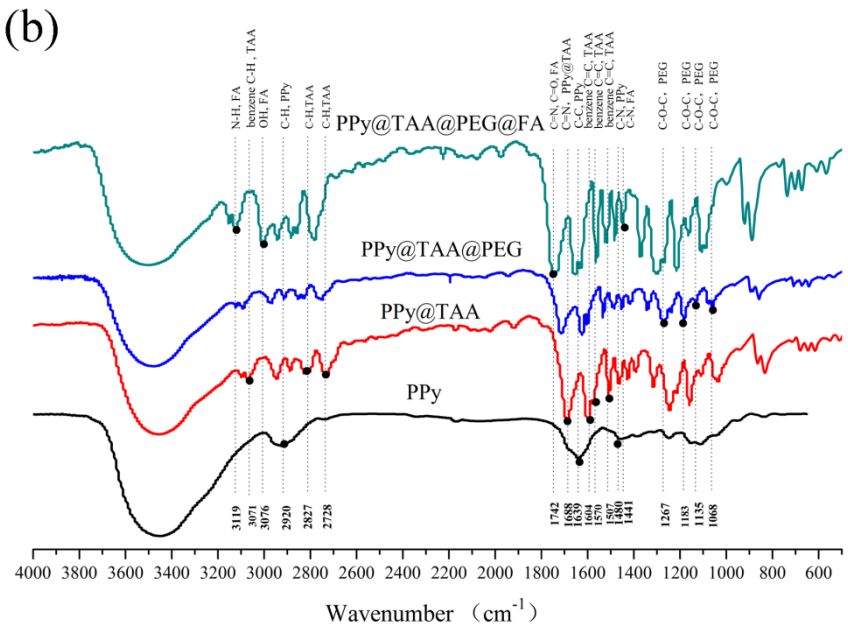

10.1002/chem.201702945

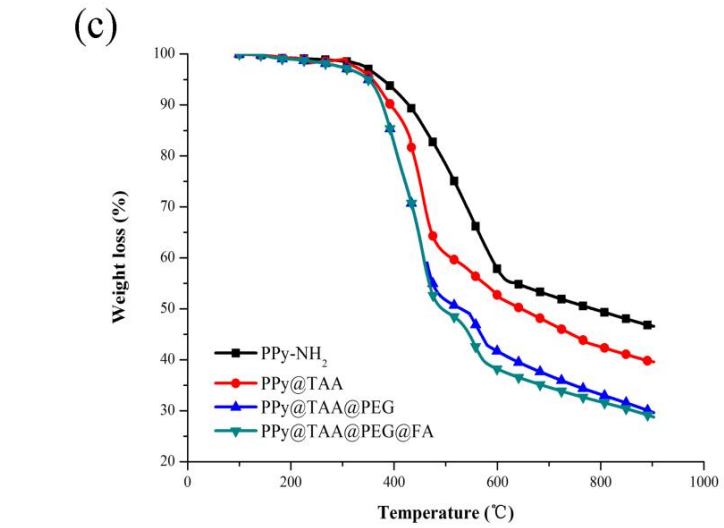

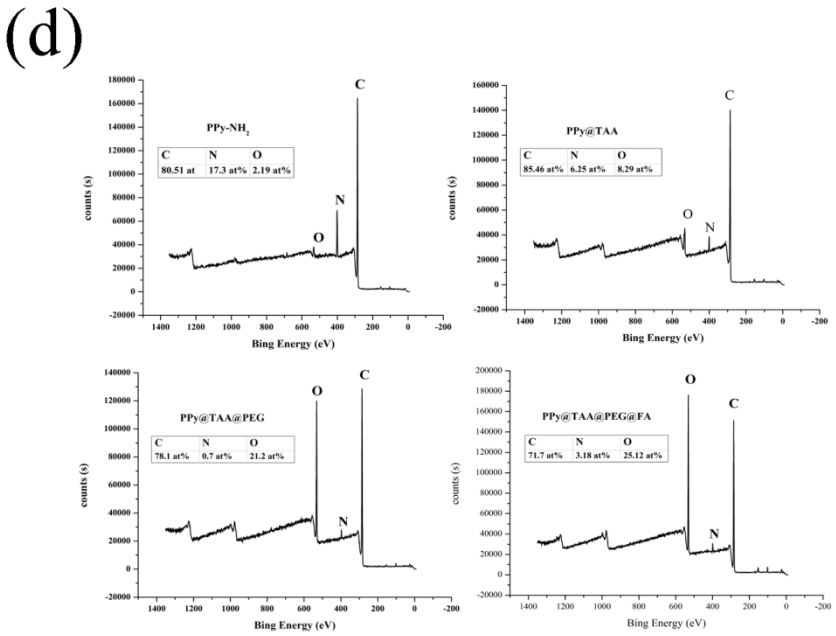

Figure 1 (a) TEM images (top) of PPy nanotubes (I, II, III, IV, and V) with the corresponding scanning electron microscopy (SEM) images (bottom) of different TiO_2 nanotubes template dimensions as well as the schematic of template method (middle). (b) FT-IR spectra of PPy, PPy@TAA, PPy@TAA@PEG, and PPy@TAA@PEG@FA. (c) TGA curves of PPy, PPy@TAA, PPy@TAA@PEG, and PPy@TAA@PEG@FA. (d) XPS spectra of PPy, PPy@TAA, PPy@TAA@PEG, and PPy@TAA@PEG@FA.

α-FR Expression Level Evaluation between Tumor Cells and Normal Cells. In

10.1002/chem.201702945

order to verify the FA targeting capability of the prepared nanoparticles, cell surface α-FR expression was first assessed. The expression of α-FR protein on the tumor cells was investigated with western blotting[35] using a highly specific polyclonal antibody. Two clear α-FR protein bands were observed for tumor cells (human ovarian carcinoma (Skov3) cells) but was negligible for normal cells (human embryonic kidney (HEK 293T) cells) (Figure 2). To gain further insight on α-FR expression, we analyzed the effect in microRNA (miRNA) level. qPCR is a sensitive technique to estimate the expression level of circulating miRNAs[36], with reference genes being used as an internal control (β -actin) for reliable normalization of target miRNA data. qPCR analysis showed a significantly higher α-FR mRNA (*FOLR1*)[37] level in Skov3 compared with HEK 293T, a result consistent with the western blot analysis (Figure 2). Therefore, the high levels of *FOLR1* gene expression led to high α-FR protein levels.

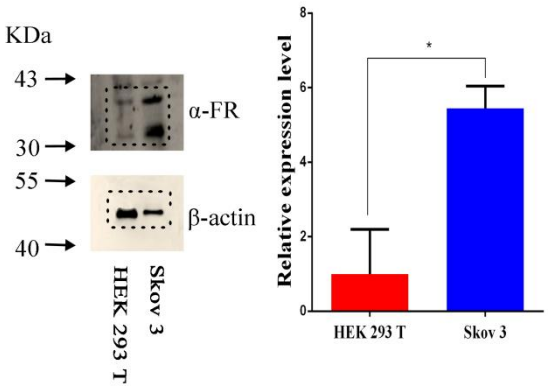

Figure 2. Assessment of α-FR protein expression in Skov3 and HEK 293T cells using western blotting (molecular weight markers were noted and the bands were indicated by dashed boxes) and relative expression levels of *FOLR1* gene determined by qPCR. *P* values of less than 0.05 were considered significant (*$P < 0.005$). β -actin is used to normalize protein expression due to its high conservation as an endogenous housekeeping gene.

***In Vitro* Cell Uptake of Different Sized Nanoparticles.** In order to verify the tumor-targeted uptake capacity of different sized nanoparticles in tumor cells, flow

10.1002/chem.201702945

cytometry analysis was carried out to quantitatively evaluate the cellular uptake behavior of different sized coumarin-6-labeled PPy@TAA@PEG@FA nanoparticles according to mean fluorescence intensity (MFI) in the two cell lines (Skov3 and HEK 293T) (Figure 3). In order to assess cell uptake of nanoparticles according to particle size, the incubation time and coumarin-6 concentration were fixed. For Skov3 cells, PPy@TAA@PEG@FA (Ⅰ) had a MFI value of 3834, approximately 1.44-fold higher than that of PPy@TAA@PEG@FA (Ⅴ), having efficient interfacial interaction with the cell membrane and suggesting prominent cellular uptake of the smaller sized nanoparticles. The Skov3 cellular uptake of PPy@TAA@PEG nanoparticles was at a low MFI, indicating that nanoparticles unconjugated FA could not interact with α-FR of Skov 3 cells. Regardless of particle size, no obvious fluorescence was observed from HEK 293T incubated with PPy@TAA@PEG and PPy@TAA@PEG@FA nanoparticles. Certainly, the two cell lines decelerated the internalization of PPy@TAA@PEG nanoparticles attributed to non-specific endocytosis. Therefore, the selectivity of PPy@TAA@PEG@FA for tumor cells over normal cells was high, in particular for smaller sized nanoparticles, due to the overexpression of α-FR on the surface of Skov3.

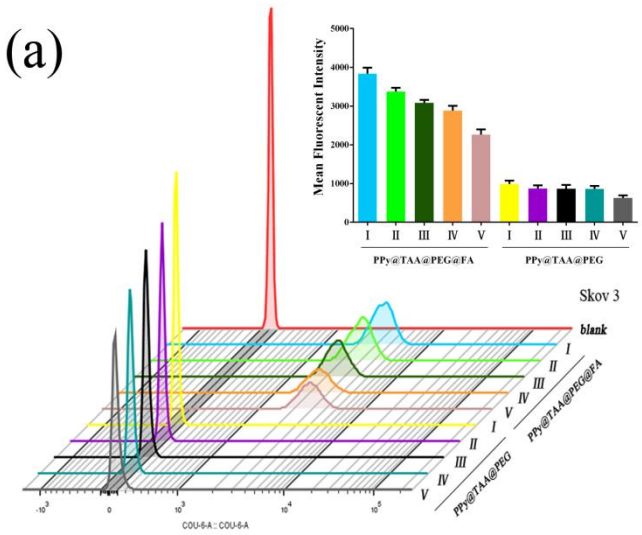

10.1002/chem.201702945

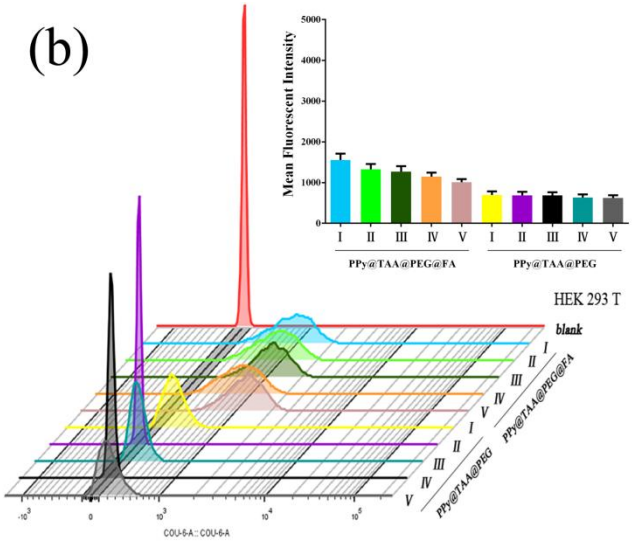

Figure 3. Flow cytometry analysis of Skov3 (a) and HEK 293T (b) cells treated with different sized coumarin-6-labelled nanoparticles for 12 h. Each bar represents the mean ± SD (n = 3).

Following quantitative measurement of the cellular uptake of the different sized nanoparticles, qualitative analysis demonstrated the cellular association of coumarin-6-labelled nanoparticles in a time-dependent manner under a fluorescent microscope (Figure 4 and Supporting Information Figure S 8). The smaller the PPy@TAA@PEG@FA nanoparticles size, the faster the cellular uptake by Skov3 cells, especially for nanoparticles I and II (Figure 4 (a, b)), while far less PPy@TAA@PEG nanoparticles were internalized in Skov3 cells (Figure S 8 (a, b)). These results also indicate that the presence of the FA motif improved the nanoparticles' ability to bind onto the tumor cells, leading to enhanced cellular uptake. As expected, a rather feeble fluorescence in HEK 293T cells was observed as a function of time regardless of treatment with PPy@TAA@PEG@FA or PPy@TAA@PEG nanoparticles. This was attributed to the rare internalization and not easily hydrolyzing aromatic imine bond of these nanoparticles in HEK 293T cells. Thus, the smaller nanoparticles exhibited a noticeable enhancement in tumor cell uptake , which is consistent with the results of flow cytometry. The still weak fluorescence was observed after 24 h incubation in Supporting Information Figure S 8

10.1002/chem.201702945

(a, d) , which could be the ascribed to cells desquamation and fluorescence quenching of coumarin-6. Nevertheless, the nanoparticles I system exhibited the lowest drug loading (only 6.15 wt%, Table S 2) and was therefore not used for the follow-up experiments. Instead, the nanoparticles II system (180 nm hydrodynamic size) were chosen, which had a reasonable size, suitable drug loading, and the efficient cellular uptake.

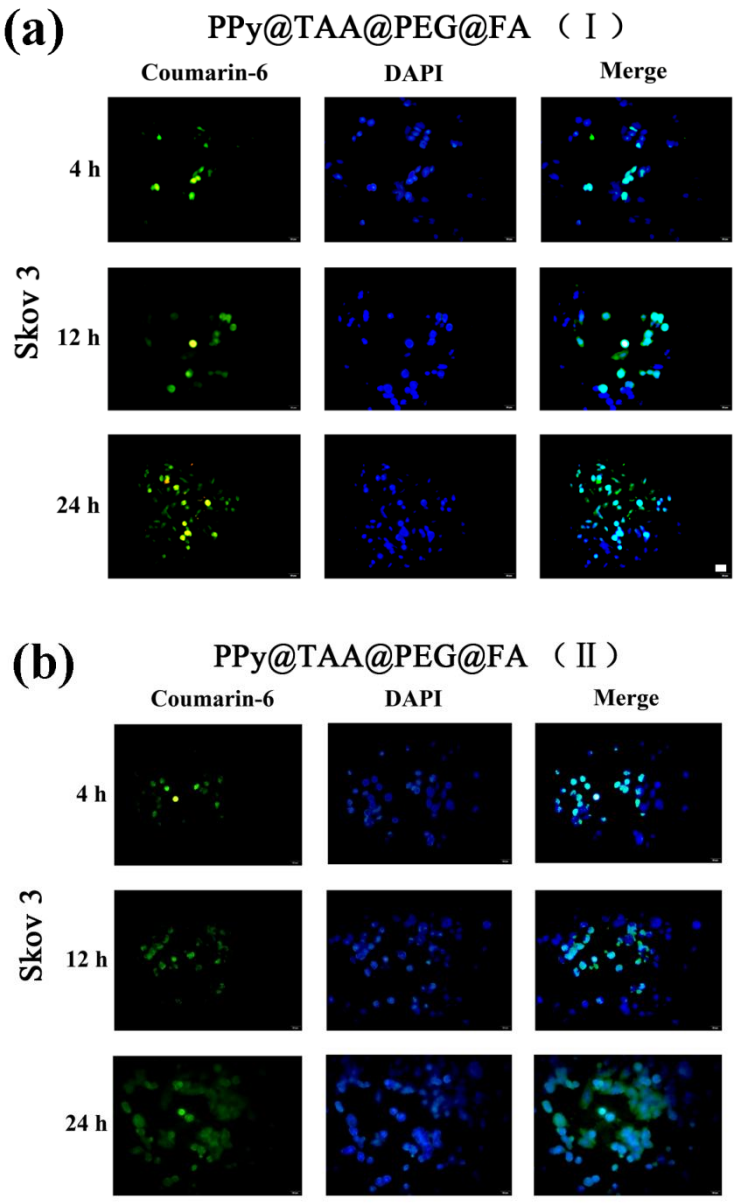

10.1002/chem.201702945

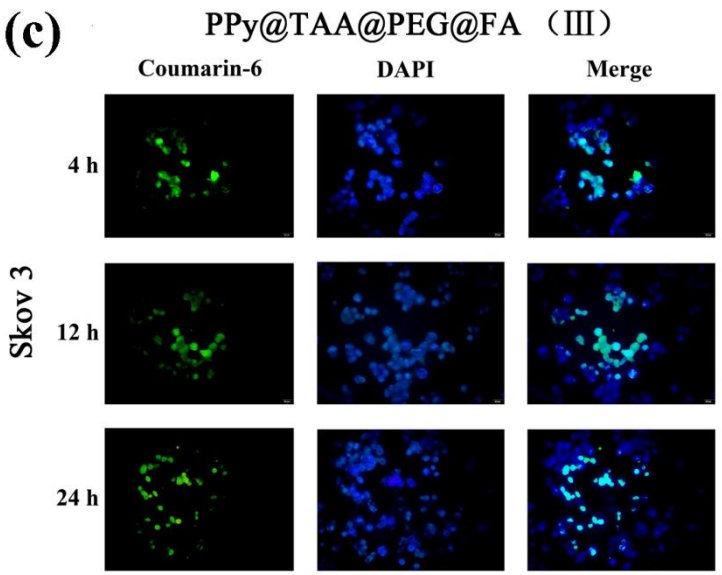

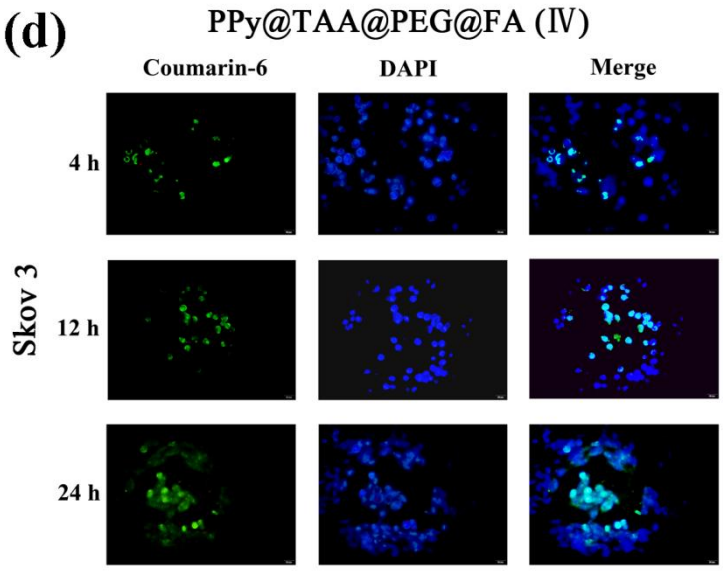

10.1002/chem.201702945

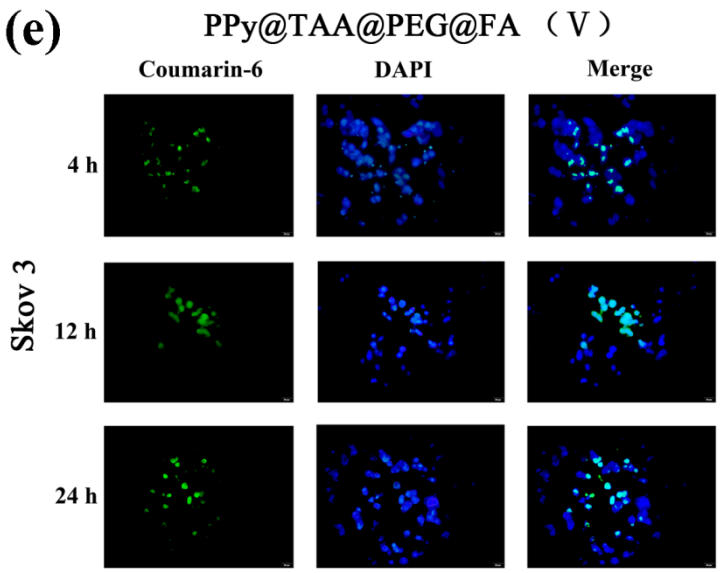

Figure 4. fluorescence images of Skov3 cells incubated with coumarin-6-loaded PPy@TAA@PEG@FA under different indicated times. Coumarin-6-loaded nanoparticles appeared in green and the nuclei stained with DAPI in blue, Scale bars: 20 μm.

***In Vitro* Release of Dox from Nanoparticles.** The release behavior of Dox-loaded nanoparticles was discussed in medium of different pH values (pH 2.5, 4.5, 6.5, 7.4, 8.0, and 9.1). As shown in Figure 5 (a), the release behavior of nanoparticles showed a clear pH-dependent feature: the lower the pH, the faster the drug release. The accumulative Dox release was approximately 80% at pH 2.5 after 15 h, with similar release profiles at pH 4.5 and 6.5 (simulating the pH of endosome and lysosome, respectively). At these pH values, the assembled nanostructure would dissociate due to cleavage of the aromatic imine bond. To be more specific, the hydrophobic TAA shell attached onto the PPy nanotubes surface would maintain Dox within a hydrophobic chamber, and be hydrolyzed in an acidic aqueous environment gradually. Interestingly, no significant burst release was observed at pH 7.4 (simulating the pH of blood), 8.0, and 9.1, and only less than 10% of Dox leaked out throughout the 40-h period. Yet, after acidification of the medium, the drug was released (Figure 5 (b)), indicating the relatively robust host-guest interactions of the nanocarrier. Therefore, drug encapsulation at physiological conditions (pH 7.4) would minimize premature

drug leakage in the blood circulation before reaching tumor tissues, resulting not only in reduced systemic toxicity but also in enhanced drug bioavailability at the target sites.

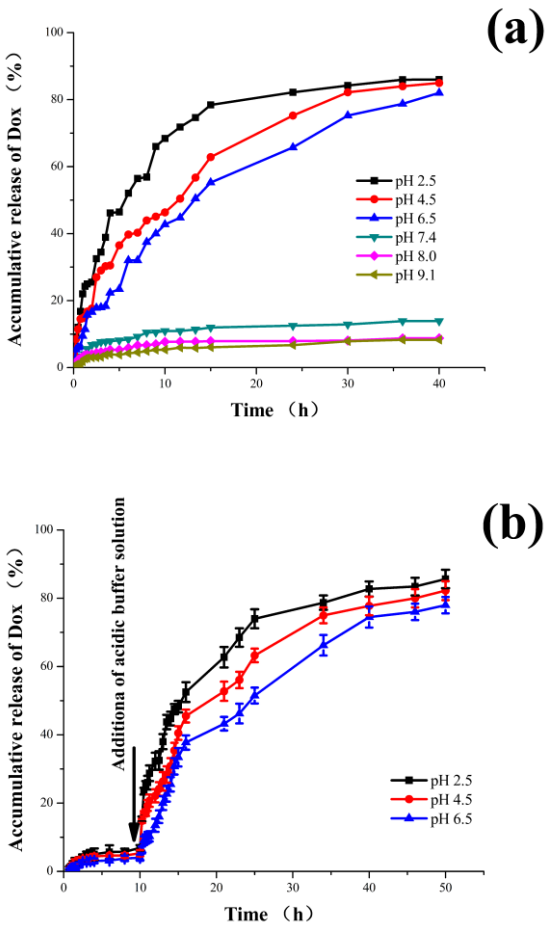

Figure 5. Release behavior of Dox-loaded nanoparticles in the buffer solution at different pH values (a) and release behavior of Dox-loaded nanoparticles in the buffer solution (pH 7.4) triggered by the addition of different acidic pH values buffer solution (b). Data are presented as mean ± SD (n = 3).

***In Vitro* Cytotoxicity of Nanoparticles and Antitumor Effect of Dox Loaded Nanoparticles.** To determine whether the nanoparticles were a safe and efficient drug vehicle, the *in vitro* cytotoxicity of nanoparticles was evaluated through cell viability against the Skov3 and HEK 293T cells using a CCK-8 assay (Figure 6 (a, b)). Given that the nanoparticles would dissociate during circulation, the two cell lines were exposed to serial nanoparticles concentrations of the various functionalizations,

namely PPy, PPy@TAA, PPy@TAA@PEG, and PPy@TAA@PEG@FA, for 24 h to evaluate their individual toxicity. The drug-free nanoparticles with different functionalization showed no or low cytotoxicity, even up to the highest testing concentration of 2000 μg/mL (Figure 6 (a, b)), indicating their excellent biocompatibility.

Following verification of the safety of the nanoparticles, The cell growth inhibitory effect of Skov3 and HEK 293T cells treated with free Dox or an equivalent dose of Dox-loaded onto either PPy@TAA@PEG or PPy@TAA@PEG@FA was observed (Figure 6 (c, d)). The cytotoxic efficacy of Dox/PPy@TAA@PEG@FA against Skov3 cells was higher than that of Dox/PPy@TAA@PEG, indicating that the targeting of the nanoparticles to Skov3 cells through FR-mediated endocytosis enhanced the internalization of nanoparticles and hence led to a significant percentage of Dox release. In addition, the IC_{50} (half maximal inhibitory concentration) of Dox against Skov3 was 1.126 μg/mL, while that of Dox/PPy@TAA@PEG@FA was 6.594 μg/mL. According to their IC_{50}, the toxic effect of Dox/PPy@TAA@PEG@FA was significantly lower than that of free Dox for the reason that Dox could easily cross the tumor cell membrane via free diffusion, while Dox/PPy@TAA@PEG@FA required endocytosis and traded with acidic endosomes/lysosomes to release the drug. Furthermore, the release of Dox from PPy@TAA@PEG@FA was pH-sensitive as indicated by the *in vitro* release studies, with less than 20% of the total Dox not being released after 24 h (Figure 6 (b)). To further evaluate the selectivity of Dox/PPy@TAA@PEG@FA against tumor cells over normal cells, the cell viability of HEK 293T cells treated with free Dox, Dox/PPy@TAA@PEG, and Dox/PPy@TAA@PEG@FA was assessed at different Dox doses. HEK 293T cells were less sensitive to Dox/PPy@TAA@PEG@FA compared with Skov3 cells, while both of them were equally sensitive to free Dox. The selective tumor cell growth inhibition could be attributed to the cooperative effects of the right nanoparticles size, FA-mediated endocytosis, and pH-triggered Dox release. In addition, the drug-free nanoparticles tested at high concentrations caused no obvious cytotoxicity towards the Skov3 cells, indicating that the cytotoxicity was only ascribed to the release of Dox

10.1002/chem.201702945

from nanoparticles rather than from the nanoparticles themselves.

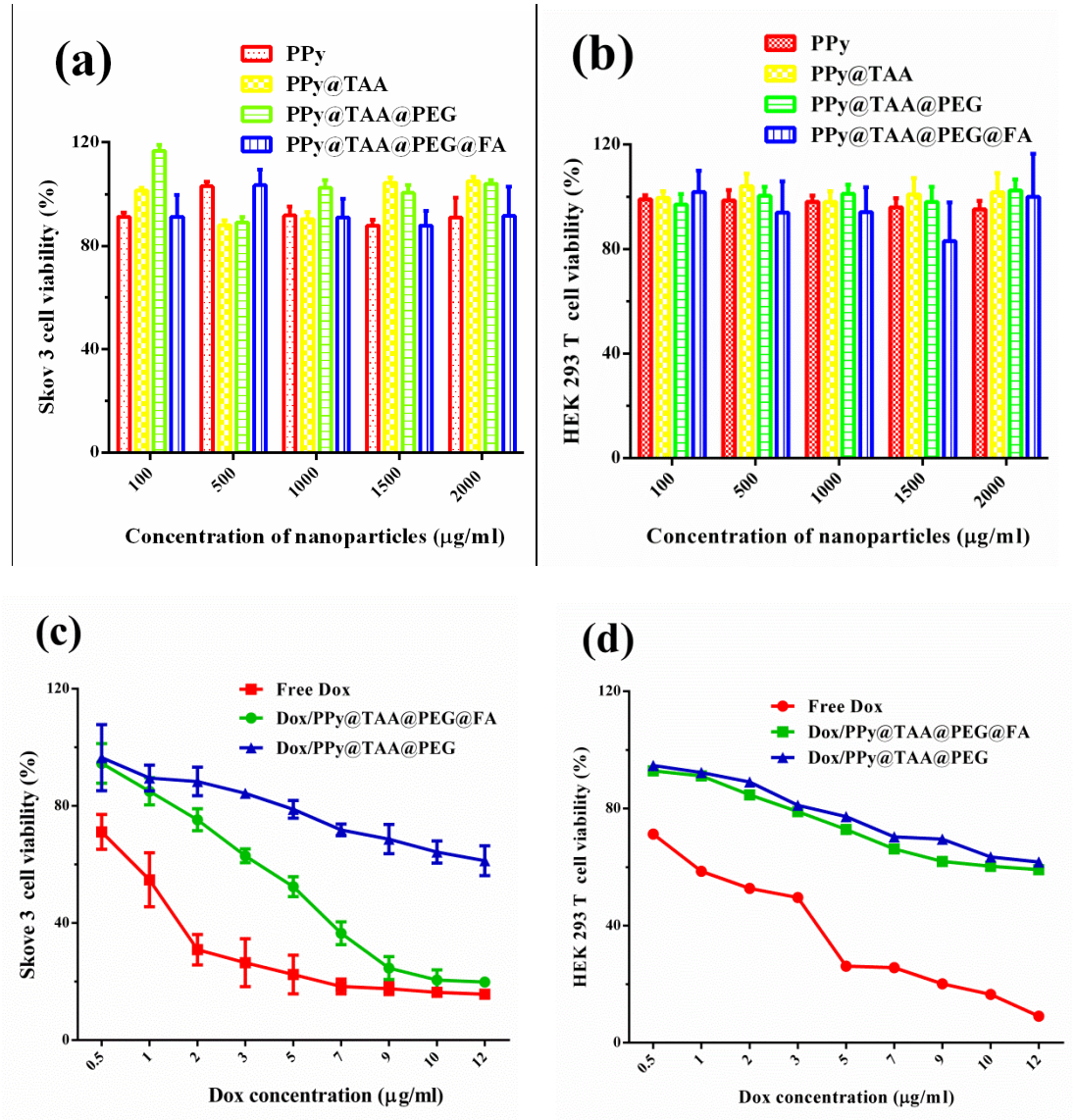

Figure 6. Cell viability of Skov3 and HEK 293T cells following incubation with as prepared (a, b) and Dox-loaded (c, d) nanoparticles at equivalent Dox concentrations for 24 h. Data were presented as mean ± SD (n = 6).

***In Vivo* Biodistribution of Nanoparticles.** To investigate the potential of PPy@TAA@PEG@FA nanoparticles to specifically deliver drugs to tumor tissues, the biodistribution of Dir-loaded nanoparticles (9.3 % Dir for PPy@TAA@PEG@FA and 9.62 % Dir for PPy@TAA@PEG) in tumor xenograft mice was evaluated by real-time fluorescence monitoring. As shown in Figure 7, the fluorescence signal of Dir/PPy@TAA@PEF@FA in the tumor region was weak at 4 h, sensible at 12 h, and

10.1002/chem.201702945

strong at 24 h. Additionally, the tumor and main organs were dissected from mice after 24 h and the strongest fluorescence intensity was observed in the tumor tissue, indicating that the PPy@TAA@PEG@FA nanoparticles were stable during blood circulation and were accumulated into the tumor with a long retention time. In contrast, the biodistribution of PPy@TAA@PEG nanoparticles was relatively spread out in mice, as observed by the relatively strong fluorescence intensity in tumor and liver tissue, due to the passive nanoparticles accumulation in tumors by the EPR effect and the liver being the main metabolism organ for elimination in mice. Thus, the prepared nanoparticles showed superior tumor-targeting capability with negligible accumulation in non-tumor regions.

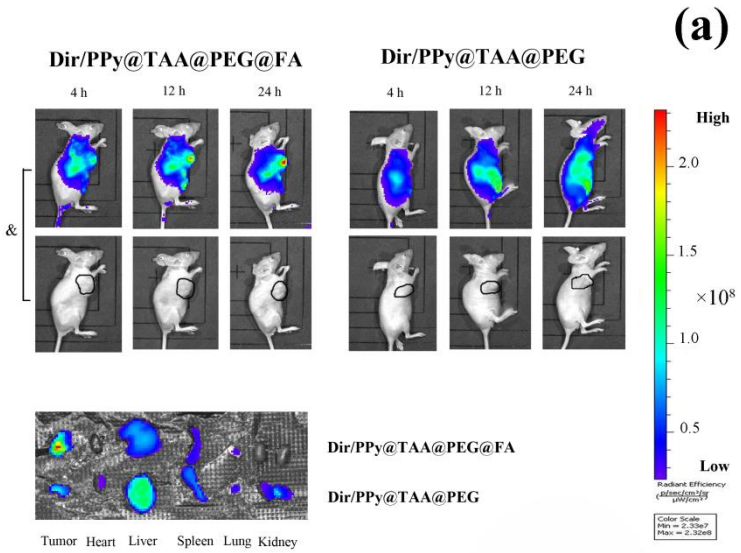

10.1002/chem.201702945

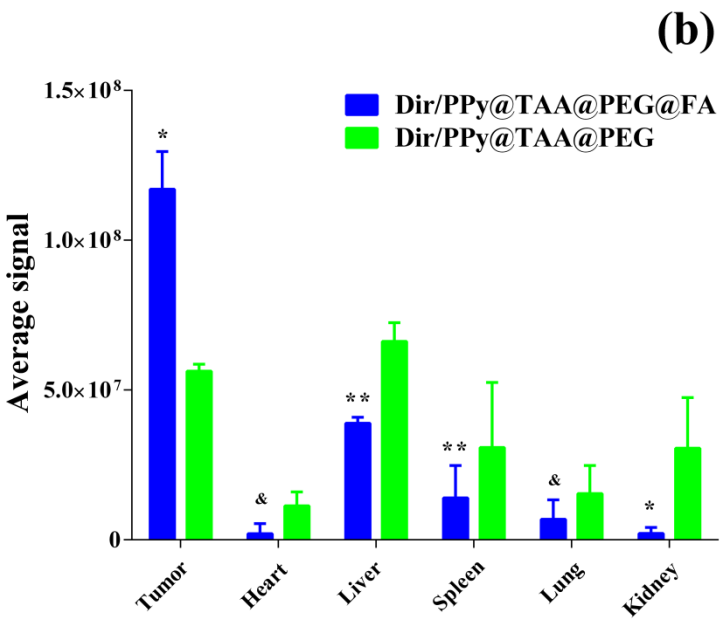

Figure 7. *In vivo* fluorescence imaging and biodistribution analysis of Dir loaded PPy@TAA@PEG@FA and Dir loaded PPy@TAA@PEG nanoparticles in tumor-bearing nude mice. (a) The time-dependent images of whole body showing the distritution of nanoparitcles and *ex vivo* fluorescence images of major organs and tumors after injection of nanoparticles at 24 h. &, the fluorescence images (upside) correspond to the optical photographs (downside). The tumors are circled with black line. (b) Quantitative biodistribution of Dir loaded PPy@TAA@PEG@FA and Dir loaded PPy@TAA@PEG nanoparticles in nude mice at 24 h. **P* <0.01; ***P* <0.05; $^{\&}$, not significant, as compared with PPy@TAA@PEG group.

Dox Loaded Nanoparticles to Inhibit Tumor Growth in a Skov 3 Tumor-bearing Nude Mouse Model. The relative tumor volume and tumor weight are shown in Figure 8 (a, b) and Supporting Information Figure S 9. All the drug-treated groups were effective in preventing tumor growth compared to PBS alone from the second therapy. The PPy@TAA@PEG@FA group exhibited the greatest tumor inhibitory effect after 21 days treatment, with a relative tumor volume reduction of 557.1%. The PPy@TAA@PEG@FA group resulted in a tumor weight of 0.2 g, showing the lowest tumor growth. This suggested a strong antitumor efficacy and consistented with the in vitro cytotoxicity assay (Figure 6 (c)). Additionally, the

PPy@TAA@PEG group was also effective in tumor growth inhibition, but less than the PPy@TAA@PEG@FA group. The free-Dox group only showed moderate antitumor efficacy. Such differences demonstrate that PPy@TAA@PEG@FA and PPy@TAA@PEG of 180 nm (hydrodynamic size) are ideal for passive accumulation into tumor tissues via the EPR effect and that active FA targeting of PPy@TAA@PEG@FA nanoparticles improved tumor particle accumulation.

The body weight of mice in the free-Dox group was unchanged along with successive administration and the skin of mice was rough during the late period of treatment (Figure 8 (c) and Figure S 9). Dox is an effective anticancer agent widely used in clinical therapy. However, the high level of Dox in normal organs generates toxic side effects, such as cumulative cardiotoxicity, myelosuppression, and nephrotoxicity, leading to stop weight gain, as described in the above result. Compared to the free-Dox group, the bodyweight of the PPy@TAA@PEG@FA and PPy@TAA@PEG groups increased over the 21-day treatment, indicating that Dox-loaded nanoparticles may effectively reduce the side effects of Dox. The large tumors lead to bodyweight loss of mice in the PBS group (7.1% bodyweight loss from initial weight) during the late period. The above data confirms that the appropriate size (Figure 1 (a) and Table S 2), their effective encapsulation of Dox (Figure 5), and low level systemic toxicity of the nanoparticles (Figure 6 (a)) make these nanoparticles (PPy@TAA@PEG@FA) an effective formulation for tumor suppression.

Tissue Distribution Studies in Tumor-bearing Mice. The total Dox levels in tumor, heart, liver, spleen, lung, and kidney after free Dox or Dox-loaded nanoparticles treatment are shown in Figure 8 (d). The tissue distribution characteristics of Dox were significantly different compared with Dox/PPy@TAA@PEF@FA, Dox/PPy@TAA@PEG, and free Dox group. As anticipated, the total content of Dox in tumors for the Dox/PPy@TAA@PEG@FA group was 1.8- and 3.12-fold higher than that of the Dox/PPy@TAA@PEG and free-Dox groups, respectively. The biodistribution characteristics of the nanoparticles

10.1002/chem.201702945

were determined by the physicochemical properties of particle size and surface modification. Generally, PEGylation of nanoparticles surfaces increased their hydrophilicity and blocked electrostatic and hydrophobic interactions, resulting in decreased liver, kidney, and spleen uptake. This was attributed to steric and hydration repulsions of PEG[38]. Extensive accumulation was also observed in tumors in the Dox/PPy@TAA@PEG group, likely due to passive accumulation into tumor tissues via the EPR effect, suggesting that the appropriate particle size played a more important role in improving the nanoparticles biodistribution profiles. Contrary to a relatively strong fluorescence signal of Dir/PPy@TAA@PEG@FA and Dir/PPy@TAA@PEG group in liver (Figure 7), the low Dox accumulation of Dox/PPy@TAA@PEG@FA and Dox/PPy@TAA@PEG group in liver was attributed to acidic-trigger release of Dox-loaded nanoparticles. Even though the Dox-loaded nanoparticles were retained in liver and other organs, the Dox was not released randomly. The free-Dox group displayed considerable Dox accumulation in all the tissues but lung. Thus, in association with material characterizations (Figure 1), *in vitro* cellular uptake (Figure 3 and 4), and drug release (Figure 5) results, a longer circulation time was achieved by PEGylation, tumor accumulation of the nanoparticles occurred by passive and FA targeting, and drug release was controlled by the TAA guard.

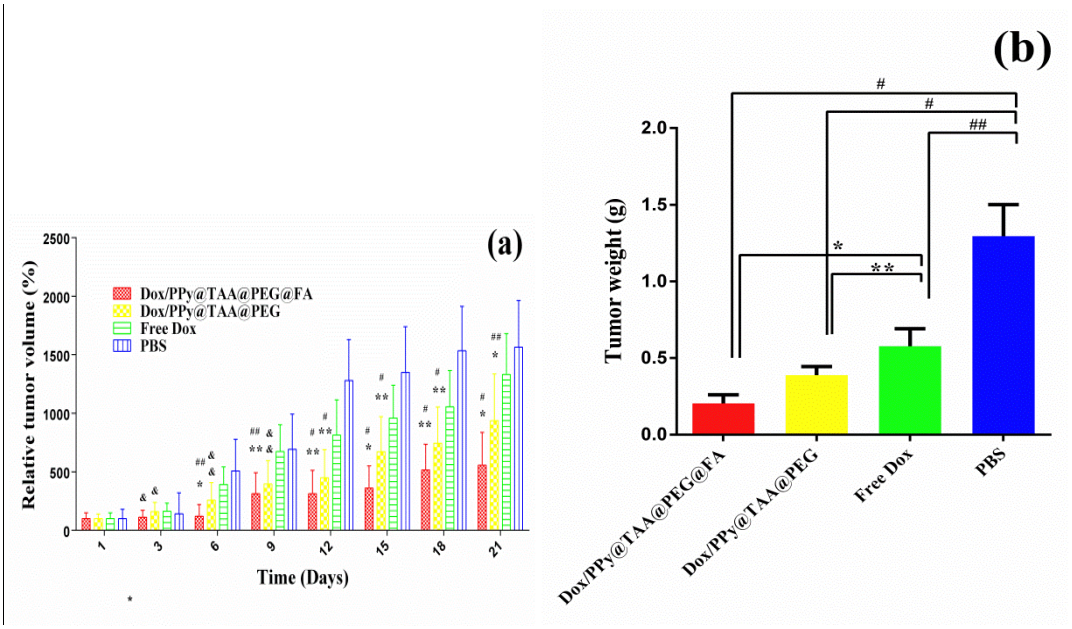

10.1002/chem.201702945

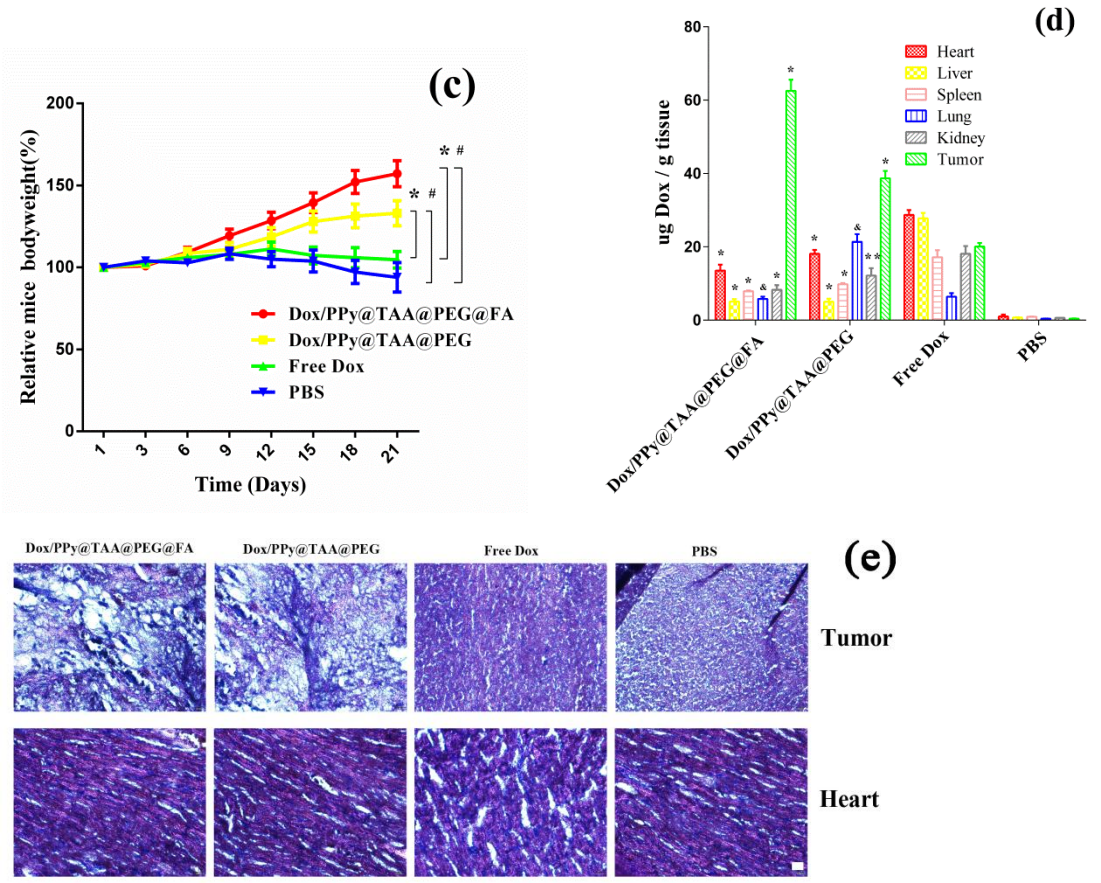

Figure 8. *In vivo* antitumor efficacy of nanoparticles in a Skov3 tumor-bearing mice model. (a) Tumor volume changes of different groups according to time. **P* <0.01; ***P* <0.05, as compared with free-Dox group; $^{\#}P$ <0.01; $^{\#\#}P$ <0.05, as compared with PBS group. (b) Bodyweight shifts from different groups. **P* <0.0001, as compared with free-Dox group; $^{\#}$P <0.0001, as compared with PBS group. (c) Tumor weight after 21 days treatment. **P* <0.0005; ***P* <0.05, as compared with free-Dox group; $^{\#}P$ <0.001, $^{\#\#}P$ <0.0005, as compared with PBS group. (d) Distribution profiles of total Dox in tissues after intravenous administration of Dox-loaded nanoparticles n = 5; $^{\&}$, not significant; **P* <0.0001; ***P* <0.005, as compared with free-Dox group. All data were expressed as mean ± SD, n = 5. (e) Hematoxylin and eosin stained with tumor and heart sections. Nuclei were stained blue and cytoplasm were stained red, Scale bars: 20 μm.

Histological Analysis. Histological analysis also supported the excellent therapeutic effect of the nanoparticles. As shown in Figure 8 (e), tumors treated with

free-Dox and PBS generally consisted of tightly packed tumor cells and some necrotic regions as a result of fast tumor cell growth. However, extensive fragmentation and nuclear shrinkage were observed in the Dox/PPy@TAA@PEG@FA and Dox/PPy@TAA@PEG group tumors. This is attributed to the advantages of nanoparticles: (1) the potential stability in blood circulation, (2) efficient delivery of Dox into the tumor cells, and (3) the high intracellular drug concentration to inhibit tumor cell growth. To evaluate the myocardial damage induced by the Dox treatments, histological changes of cardiomyocytes were observed. The Dox/PPy@TAA@PEG@FA, Dox/PPy@TAA@PEG, and PBS groups showed no significant morphological changes and had compact cardiomyocytes in an ordered arrangement with clear structures. However, the free-Dox group exhibited disordered myofibrillar structures, characterized by acute myocardial damage.

CONCLUSION

In summary, taking advantage of the template method, different size PPy@TAA@PEG@FA nanoparticles were synthesized. The physicochemical characteristics of the nanoparticles were determined by TEM, FT-IR, TGA, and DLS. Flow cytometry and fluorescence imaging analyses showed that cellular uptake exhibited size effect and targeting effect, and PPy@TAA@PEG@FA nanoparticles of 180 nm hydrodynamic size had higher Skov3 cell internalization. *In vitro* cytotoxicity assays confirmed that Dox/PPy@TAA@PEG@FA nanoparticles induced Skov3 tumor cell death. *In vivo* studies demonstrated that Dox-loaded PPy@TAA@PEG@FA nanoparticles exhibited the highest antitumor activity, followed by PPy@TAA@PEG, compared to free Dox. Importantly, we successfully developed and used the PPy model as a drug carrier. The nanoparticles design combines the size effect as well as active targeting, opening up a new path to the establishment of functionalized drug nanocarriers. Further improvements on the nanoconstruction should focus on the drug loading capacity of the system.

ACKNOWLEDGEMENTS

This project is financially supported by the National Natural Science Foundation of China (No. 21276283, 21576295, 81201675 and 81572900) and the Open-End Fund for the Valuable and Precision Instruments of Central South Univeristy (CSUZC201725). We thank the MRI facility of Modern Analysis and Testing Center of Central South University for technical support.

REFERENCES

[1] K. Riehemann, S. W. Schneider, T. A. Luger, B. Godin, M. Ferrari and H. Fuchs, *Angew. Chem. Int. Ed.* **2009**, *48*, 872-897.

[2] X. Lin, N. Zhao, P. Yan, H. Hu and F. J. Xu, *Acta Biomater.* **2015**, *11*, 381-392.

[3] G. A. Hughes, *Nanomedicine* **2005**, *1*, 22-30.

[4] Z. Y. Li, J. J. Hu, Q. Xu, S. Chen, H. Z. Jia, Y. X. Sun, R. X. Zhuo and X. Z. Zhang, *J. Mater. Chem. B* **2015**, *3*, 39-44.

[5] S. S. Han, Z. Y. Li, J. Y. Zhu, K. Han, Z. Y. Zeng, W. Hong, W. X. Li, H. Z. Jia, Y. Liu, R. X. Zhuo and X. Z. Zhang, *Small* **2015**, *11*, 2543-2554.

[6] Y. Hu, J. Chen, X. Li, Y. Sun, S. Huang, Y. Li, H. Liu, J. Xu and S. Zhong, *Nanotechnology* **2017**, *28*, 375101.

[7] R. V. Chari, M. L. Miller and W. C. Widdison, *Angew. Chem. Int. Ed.* **2014**, *53*, 3796-3827.

[8] F. Xu, J. Liu, J. Tian, L. Gao, X. Cheng, Y. Pan, Z. Sun and X. Li, *ACS Appl. Mater. Interfaces* **2016**, *8*, 29906-29914.

[9] a) W. Zhang, Z. L. Yu, M. Wu, J. G. Ren, H. F. Xia, G. L. Sa, J. Y. Zhu, D. W. Pang, Y. F. Zhao and G. Chen, *ACS nano* **2017**, *11*, 277-290; b) N. C. Fan, F. Y. Cheng, J. A. Ho and C. S. Yeh, *Angew. Chem. Int. Ed.* **2012**, *51*, 8806-8810; c) S. A. Kularatne, V. Deshmukh, M. Gymnopoulos, S. L. Biroc, J. Xia, S. Srinagesh, Y. Sun, N. Zou, M. Shimazu, J. Pinkstaff, S. Ensari, N. Knudsen, A. Manibusan, J. Y. Axup, C. H. Kim, V. V. Smider, T. Javahishvili and P. G. Schultz, *Angew. Chem. Int. Ed.* **2013**, *52*, 12101-12104; d) S. K. Jones, V. Lizzio and O. M. Merkel, *Biomacromolecules* **2016**, *17*, 76-87.

[10] M. C. Planca-wessels, G. C. Booth, A. J. Convertine, B. B. Lundy, G. Y. Berguig, M. F. Press, P. S. Stayton and O. W. Press, *Oncotarget* **2016**, *7*, 9561-9575.

[11] C. O. Evans, P. Reddy, D. J. Brat, E. B. O'Neill, B. Craige, V. L. Stevens and N. M. Oyesiku, *Cancer Res.* **2003**, *63*, 4218-4224.

[12] J. A. Ledermann, S. Canevari and T. Thigpen, *Ann. of Oncol.* **2015**, *26*, 2034-2043.

[13] a) L. Yan, B. Zhao, X. Liu, X. Li, C. Zeng, H. Shi, X. Xu, T. Lin, L. Dai and Y. Liu, *ACS Appl. Mater. Interfaces* **2016**, *8*, 6834-6840; b) Z. F. Zhou, F. Zhang, J. G. Wang, Q. C. Chen, W. C. Yang, W. Z. Yang, N. He, Y. Y. Jiang, F. Chen and J. J. Liu, *ACS Biomater. Sci. Eng.* **2016**, *2*, 1572-1581.

[14] a) N. Hosseini Nassab, D. Samanta, Y. Abdolazimi, J. P. Annes and R. N. Zare, *Nanoscale* **2017**, *9*,

143-149; b) D. Uppalapati, B. J. Boyd, S. Garg, J. Travas-Sejdic and D. Svirskis, *Biomaterials* **2016**, *111*, 149-162.
[15] Q. Li, C. Yu, R. Gao, C. Xia, G. Yuan, Y. Li, Y. Zhao, Q. Chen and J. He, *Biosens. Bioelectron.* **2016**, *80*, 674-681.
[16] S. H. Bauquier, K. J. McLean, J. L. Jiang, R. C. Boston, A. Lai, Z. Yue, S. E. Moulton, A. J. Halliday, G. Wallace and M. J. Cook, *Macromol. Biosci.* **2017**, *17*.
[17] Y. Wang, Y. Xiao and R. Tang, *Chem. Eur. J.* **2014**, *20*, 11826-11834.
[18] M. Zhang, T. Wang, L. Zhang, L. Li and C. Wang, *Chem. Eur. J.* **2015**, *21*, 16162-16171.
[19] D. Samanta, J. L. Meiser and R. N. Zare, *Nanoscale* **2015**, *7*, 9497-9504.
[20] P. M. George, D. A. LaVan, J. A. Burdick, C. Y. Chen, E. Liang and R. Langer, *Adv. Mater.* **2006**, *18*, 577-581.
[21] G. Chen and C. Mao, *Nanoscale* **2016**, *8*, 10026-10029.
[22] J. Zhang, Y. Li, F. F. An, X. Zhang, X. Chen and C. S. Lee, *Nano Lett.* **2015**, *15*, 313-318.
[23] Q. Zhang, F. Liu, K. T. Nguyen, X. Ma, X. Wang, B. Xing and Y. Zhao, *Adv. Funct. Mater.* **2012**, *22*, 5144-5156.
[24] a) S. Y. Li, L. H. Liu, H. Z. Jia, W. X. Qiu, L. Rong, H. Cheng and X. Z. Zhang, *Chem. Commun.* **2014**, *50*, 11852-11855; b) C. Y. Sun, S. Shen, C. F. Xu, H. J. Li, Y. Liu, Z. T. Cao, X. Z. Yang, J. X. Xia and J. Wang, *J. Am. Chem. Soc.* **2015**, *137*, 15217-15224; c) S. S. Han, Z. Y. Li, J. Y. Zhu, K. Han, Z. Y. Zeng, W. Hong, W. X. Li, H. Z. Jia, Y. Liu, R. X. Zhuo and X. Z. Zhang, *Small* **2015**, *11*, 2543-2554.
[25] a) N. C. Fan, F. Y. Cheng, J. A. Ho and C. S. Yeh, *Angew. Chem. Int. Ed.* **2012**, *51*, 8806-8810; b) W. Chen, J. Ouyang, H. Liu, M. Chen, K. Zeng, J. Sheng, Z. Liu, Y. Han, L. Wang, J. Li, L. Deng, Y. N. Liu and S. Guo, *Adv. Mater.* **2017**, *29*; c) K. Han, W. Y. Zhang, J. Zhang, Q. Lei, S. B. Wang, J. W. Liu, X. Z. Zhang and H. Y. Han, *Adv. Funct. Mater.* **2016**, *26*, 4351-4361.
[26] J. J. Hu, L. H. Liu, Y. Z. Li, R. X. Zhuo and X. Z. zhang, *J. Mater. Chem. B* **2016**, *4*, 1932-1940.
[27] a) Y. Wang, J. Chen, C. Zhou, L. Zhou, Y. Kong, H. Long and S. Zhong, *Electrochim. Acta* **2014**, *115*, 269-276; b) J. Chen, Y. Kang, C. Li, H. Chen, L. Sun, Y. Wang and S. Zhong, *J. Electrochem. Soc.* **2016**, *164*, B66-B73.
[28] a) D. E. Applequst, G. F. Fanta and B. W. Henrikson, *The Journal of Organic Chemistry* **1958**, *23*, 1715-1716; b) S. F. Marrian, *Chem. Rev.* **1948**, *43*, 149-202.
[29] R. Banerjee, S. Maiti and D. Dhara, *Green Chem.* **2014**, *16*, 1365-1373.
[30] Y. He, M. Lin, Z. Li, X. Liang, G. Li and J. C. Antilla, *Org. Lett.* **2011**, *13*, 4490-4493.
[31] S. Bose, T. Kuila, M. E. Uddin, N. H. Kim, A. K. T. Lau and J. H. Lee, *Polymer* **2010**, *51*, 5921-5928.
[32] Q. Zhang, F. Liu, K. T. Nguyen, X. Ma, X. Wang, B. Xing and Y. Zhao, *Adv. Funct. Mater.* **2012**, *22*, 5144-5156.
[33] a) S. Sharma, R. W. Johnson and T. A. Desai, *Biosens. Bioelectron.* **2004**, *20*, 227-239; b) C. Malitesta, I. Losito, L. Sabbatini and P. G. Zambonin, *J. Electron Spectrosc. Relat. Phenom.* **1995**, *76*, 629-634.
[34] P. Kingshott, H. Thissen and H. J. Griesser, *Biomaterials* **2002**, *23*, 2043-2056.
[35] C. O. Evans, P. Reddy, D. J. Brat, E. B. O'Neill, B. Craige, V. L. Stevens and N. M. Oyesiku, *Cancer res.* **2003**, *63*, 4218-4224.
[36] X. Fu, Y. Li, A. Alvero, J. Li, Q. Wu, Q. Xiao, Y. Peng, Y. Hu, X. Li, W. Yan, K. Guo, W. Zhou, Y. Wang, J. Liu, Y. Zhang, G. Mor, J. Wen and G. Yin, *Oncotarget* **2016**, *7*, 80633-80654.
[37] Y. Yuan, D. A. Nymoen, H. P. Dong, O. Bjorang, I. M. Shih, P. S. Low, C. G. Trope and B. Davidson, *Hum. pathol.* **2009**, *40*, 1453-1460.

10.1002/chem.201702945

[38] a) K. Knop, R. Hoogenboom, D. Fischer and U. S. Schubert, *Angew. Chem. Int. Ed.* **2010**, *49*, 6288-6308; b) J. M. Rabanel, P. Hildgen and X. Banquy, *J. Controlled Release* **2014**, *185*, 71-87.